AGU PUBLICATIONS

Geochemistry, Geophysics, Geosystems

RESEARCH ARTICLE
10.1002/2016GC006771

Key Points:
- The three-dimensional resistivity structure showed the geological structure and fluid distribution in the Ishikari Lowland
- Soft thick sedimentary rocks and localized fluids in the basement both contributed to the strain concentration
- A magmatic fluid path and its reservoir were found beneath the Quaternary caldera

Supporting Information:
- Supporting Information S1

Correspondence to:
Y. Yamaya,
y.yamaya@aist.go.jp

Citation:
Yamaya, Y., T. Mogi, R. Honda, H. Hase, T. Hashimoto, and M. Uyeshima (2017), Three-dimensional resistivity structure in Ishikari Lowland, Hokkaido, northeastern Japan—Implications to strain concentration mechanism, *Geochem. Geophys. Geosyst.*, *18*, 735–754, doi:10.1002/2016GC006771.

Received 19 DEC 2016
Accepted 6 FEB 2017
Accepted article online 10 FEB 2017
Published online 28 FEB 2017

Three-dimensional resistivity structure in Ishikari Lowland, Hokkaido, northeastern Japan—Implications to strain concentration mechanism

Yusuke Yamaya[1], Toru Mogi[2,3], Ryo Honda[4], Hideaki Hase[5], Takeshi Hashimoto[3], and Makoto Uyeshima[6]

[1]Renewable Energy Research Center, Fukushima Renewable Energy Research Institute, AIST, Koriyama, Japan, [2]Division of Sustainable Resources Engineering, Faculty of Engineering, Hokkaido University, Sapporo, Japan, [3]Institute of Seismology and Volcanology, Faculty of Science, Hokkaido University, Sapporo, Japan, [4]Tono Research Institute of Earthquake Science, Association for the Development of Earthquake Prediction, Mizunami, Japan, [5]Geothermal Energy Research & Development Co., Ltd., Tokyo, Japan, [6]Earthquake Research Institute, The University of Tokyo, Tokyo, Japan

Abstract The Ishikari Lowland on the island of Hokkaido in northeastern Japan is situated at the end of a westward-moving foreland fold-and-thrust belt from the Hidaka collision zone, where the northeastern Japan and Kurile arcs meet. This activity forms a tectonic zone under an east-west compression field in this region. A magnetotelluric resistivity survey was performed to investigate the mechanism for the strain concentration in this region. A three-dimensional (3-D) resistivity inversion showed a conductive thick sedimentary layer and an underlying resistive basement. Remarkable conductors were found in the resistive basement beneath the Ishikari-teichi-toen fault zone (ITFZ) and the Shikotsu caldera. The conductors beneath the ITFZ were interpreted as aqueous fluids that accumulated in the damaged zone in connection with the formation of pull-apart faults and horst. In contrast, the conductor beneath the Shikotsu caldera corresponds to a magmatic fluid path from the upper mantle. These features suggest that the ductile deformation in the upper crust contribute to the strain concentration in this region. The soft thick sediments allow ductile deformations to occur. Furthermore, local fluid-rich zones in the basement cause the crustal strength to be heterogeneous. These thick sediments and local fluids in the basement both contribute to the strain concentration in this region.

1. Introduction

The Ishikari Lowland, located at the boundary between western and central Hokkaido in northeastern Japan, is recognized as a crustal strain concentration zone (Figure 1a). In the southern part of the island of Hokkaido, the subducting Pacific Plate and the northeastern Japan and Kurile arcs form a triple junction. The oblique subduction of the Pacific Plate drives the westward movement of the Kurile forearc sliver, which collides with the northeastern Japan arc in the Hidaka Mountains [e.g., *Kimura*, 1986] (Figure 1a). The fold-and-thrust structure spreads westward from the Hidaka Mountains and reaches the Ishikari Lowland [e.g., *Ito*, 2000]. This activity causes significant crustal compression with the east-west axis in this region [*Hashimoto and Tada*, 1988; *Ishikawa and Hashimoto*, 1999; *Sagiya et al*., 2000; *Ohzono*, 2013]. Because the distribution of horizontal strain is quite different on either side of the lowland, this region behaves as both a geological and a mechanical boundary [*Hashimoto and Tada*, 1988].

The Ishikari-teichi-toen active fault zone (ITFZ) is located at the eastern edge of the lowland in the foreland of the fold-and-thrust belts (Figure 1b). It consists of eastward dipping thrusts that have a nearly north-south orientation and are approximately 70 km in length [*Nakata and Imaizumi*, 2002]. The most recent activity of this fault zone is estimated to have been in 1880, and the average recurrence interval is approximately 1000–2000 years [*Earthquake Research Committee*, 2010]. The magnitude of the most recent earthquake was estimated to be M7.9 based on the hypothesis that the fault zone acted as one segment [*Earthquake Research Committee*, 2010]. However, the current seismicity around this fault zone is not very high, and the hypocenters of microearthquakes occurring in the region are located at depths of only 10–25 km in the southwestern zone (Figures 9 and 10).

Regarding the mechanism for generating an inland earthquake, some studies have suggested the contribution of fluids and structural heterogeneity in the crust, which results in a strain concentration [e.g., *Iio et al*., 2002, 2004; *Hasegawa et al*., 2005]. Thus, clarifying the fluid distribution in the crust would aid the discussion

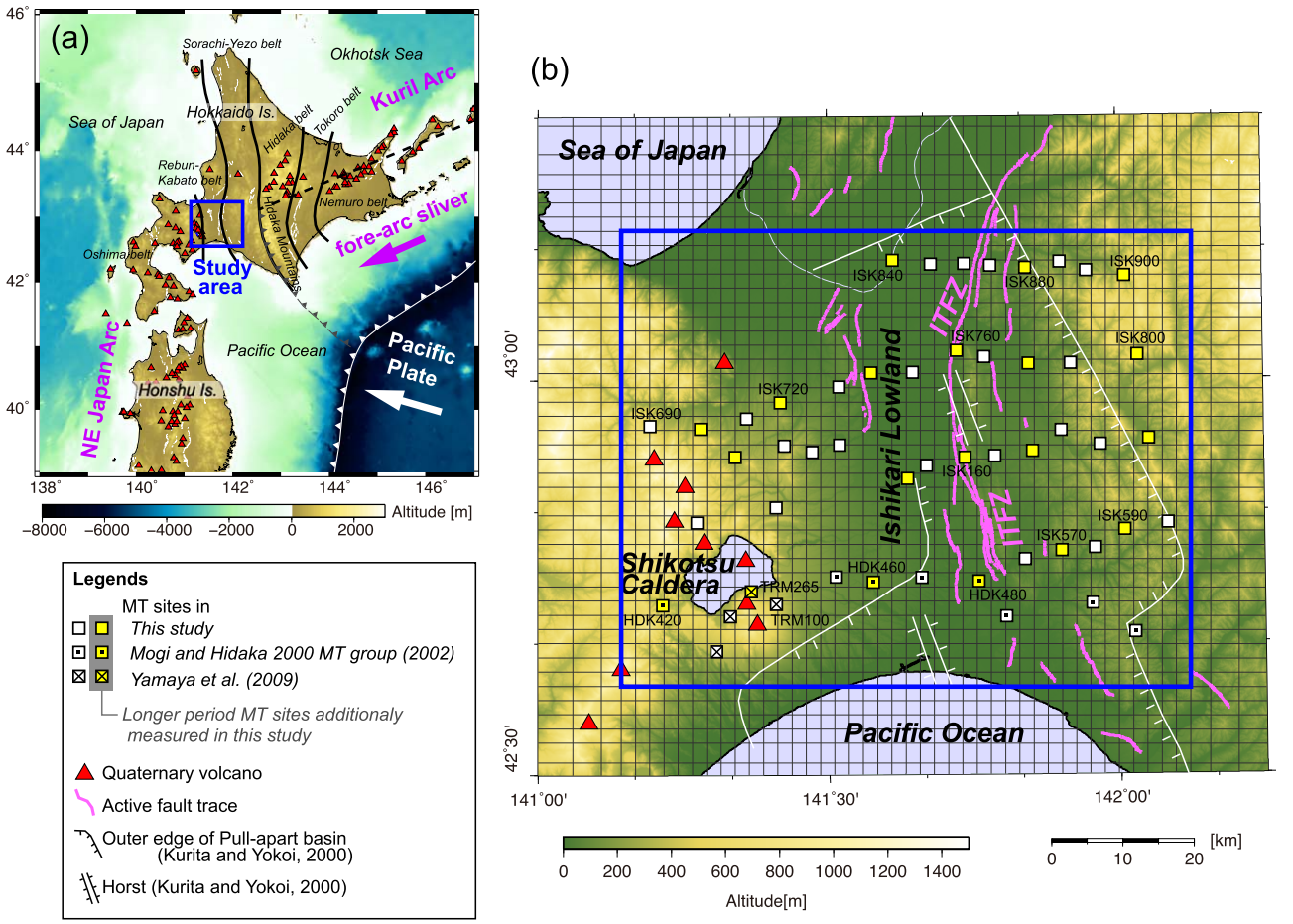

Figure 1. (a) Location of the study area. Red triangles indicate Quaternary volcanoes [*Geological Survey of Japan*, 2013]. The geological division (black line) is after *Tamaki et al*. [2010] and is a modification of that originally developed by *Kiminami et al*. [1986]. (b) Location of MT measurement sites. Squares indicates MT sites. (See the legend for more detailed definitions of the symbols.) The black mesh shows the grid design used in the 3-D inversion. The blue rectangle delineates the area shown in Figures 9 and 10. Purple lines trace active faults after *Nakata and Imaizumi* [2002]. White lines show the pull-apart basin and horst estimated by *Kurita and Yokoi* [2000].

of the mechanism of inland earthquakes, which occur in tectonic zones similar to this region. Because electrical resistivity is quite sensitive to the amount of pore fluid and its connectivity in the rocks, a subsurface resistivity structure can be used to image the fluid distribution in the crust. Many resistivity investigations in the inland earthquake zone have found electrical conductors in the lower crust beneath the active fault and high-seismicity zones [e.g., *Ogawa et al*., 2001; *Ogawa and Honkura*, 2004; *Tank et al*., 2005; *Uyeshima et al*., 2005; *Yoshimura et al*., 2008; *Ichihara et al*., 2008; *Wannamaker et al*., 2009; *Ichihara et al*., 2014]. These results support the hypothesis that the strain becomes concentrated in the upper crust above regions of the lower crust weakened by locally present fluids [e.g., *Iio et al*., 2002, 2004; *Hasegawa et al*., 2009]. Furthermore, the intrusion of such fluids into a mechanically high-strength crust could trigger earthquakes [e.g., *Ogawa et al*., 2001]. Meanwhile, the heterogeneity of the basement depth, which was clarified by the resistivity structure, could contribute to the stress concentration and the generation of inland earthquakes [*Ichihara et al*., 2008].

In this study, the magnetotelluric (MT) method was used to image the three-dimensional (3-D) resistivity structure in the Ishikari Lowland region. The basement structure and fluid distribution were estimated by interpreting the resistivity structure. The mechanism of strain concentration in this region is discussed at the end of this paper.

2. Tectonic and Geological Setting

The Ishikari Lowland has experienced drastic tectonic transitions since the Cretaceous. *Kuniyasu and Yamada* [2004] summarized the tectonic history that generated the basement structure in this region as

follows. The tectonics began as a forearc basin setting in the Cretaceous and early Paleogene. In the late Oligocene, a pull-apart basin was generated under a right-lateral transtension field and was filled by sediments. In the middle Miocene, the back-arc extension of the Sea of Japan caused an upthrust of the Hidaka belt. Consequently, the Ishikari region switched to a right-lateral transpression field and returned to the forearc basin setting. After the late Miocene and Pliocene, the activated westward-moving forearc sliver of the Kuril arc provided considerable east-west compression.

The Quaternary volcanoes, which are represented by the Shikotsu caldera, formed a volcanic zone in the western region of the Ishikari Lowland (Figure 1b). These volcanoes are located at the northern end of the volcanic front of the northeastern Japan arc. There are no volcanoes in the eastern region between the Ishikari Lowland and the volcanic front of the Kuril arc [e.g., *Hirose and Nakagawa*, 2000] (Figure 1a).

Because of the above history, the geological features of the western and eastern regions of the Ishikari Lowland region are quite different. This region belongs to the tectonic unit of the Oshima, Rebun-Kabato, and Sorachi-Ezo belts in the western, central, and eastern regions, respectively [e.g., *Kiminami et al*., 1986]. The Oshima belt corresponds to the volcanic zone of the northeastern Japan arc. The basements of the Rebun-Kabato and Sorachi-Ezo belts mainly consist of volcanic and sedimentary rocks in the Lower Cretaceous and Jurassic-Cretaceous, respectively. Based on the seismic velocity structure and logged data [*Iwasaki et al*., 2004; *Yoshida et al*., 2007], sediments above the Upper Cretaceous were largely absent in the western volcanic region, whereas they suddenly thickened in the eastern region, and the basement depths reached 8–10 km at the eastern end of the study region. Furthermore, because the arc-arc collision depressed the crust of the northeastern Japan arc, the Conrad discontinuity depths were estimated to be 15 and 25 km in the west and east, respectively [*Iwasaki et al*., 2004]. Based on the unified earthquake catalog provided by the Japan Meteorological Agency (JMA), the seismicity is concentrated at depths of 10–25 km in the southeastern region, roughly corresponding to the upper crust. Very low-frequency earthquakes occur only in the western part of the region, and their hypocenters are located at depths of 20–30 km beneath the Shikotsu caldera.

The thermal structure also shows different features in the western and eastern regions. The heat flow in the west exceeds 100 mW/m^2 as a result of the volcanic front of the northeastern Japan arc, whereas that in the east falls below 50 mW/m^2 [*Tanaka*, 2004]. In addition, the estimated solidus depths were found to be shallower than 30 km in the west, suggesting that there is partial melt in the crust [*Okubo*, 1998].

3. Magnetotelluric Method

3.1. Observation and Data Processing

MT measurements were performed in the Ishikari Lowland region in 2008, 2009, and 2010. Figure 1b shows the MT site locations, including those used in previous studies [*Mogi and Hidaka 2000 MT Group*, 2002; *Yamaya et al*., 2009]. Wideband MT measurements were performed at 39 new sites in this study. MTU-5 systems (Phoenix Geophysics, Ltd., Canada) were used to measure the time series data of two components of the electric fields and three components of the magnetic fields. The remote reference technique [*Gamble et al*., 1979] was applied to the study data and magnetic field data simultaneously obtained at the Esashi Observatory of the Geospatial Information Authority of Japan, which is approximately 400 km from the study area. SSMT 2000 software (Phoenix Geophysics, Canada) was used to calculate the MT impedance and magnetic transfer function over a period range of 3.1×10^{-3}–2.9×10^{3} s (3.4×10^{-4}–3.2×10^{2} Hz).

Previous studies have demonstrated that a thick conductive layer exists at the surface [*Mogi and Hidaka 2000 MT Group*, 2002; *Yamaya et al*., 2009]. Limitations to the sounding depth, which depends on the resistivity of the earth and the analysis period, were a concern in this study. To ensure a sufficient sounding depth, longer-period MT measurements were also performed at 20 of the wideband MT sites (yellow symbols in Figure 1b). The electromagnetic fields were measured with a sampling period of 1 s by U43 systems (Tierra Tecnica, Ltd., Japan). The obtained time series data were transformed to MT impedances and magnetic transfer functions over a period range of $16 - 1.3 \times 10^{4}$ s (7.6×10^{-5}–6.3×10^{-2} Hz) using the bounded influence remote reference processing (BIRRP) code [*Chave and Thomson*, 2004]. Magnetic field data from the Kakioka Geomagnetic Observatory (JMA), which is approximately 750 km from the study area, were used in this remote reference technique.

3.2. Data Presentation

Figure 2 shows sounding curves for the apparent resistivity and impedance phase at representative sites. The off-diagonal components show good quality, with small error bars and seamless continuity with respect to the period. The diagonal components show relatively poor quality over a band denoted the dead band, and for periods longer than the dead band. The data obtained by the MTU and U43 at the same sites were in good agreement. The U43 data were used for periods longer than 100 s because they were generally better than the MTU data.

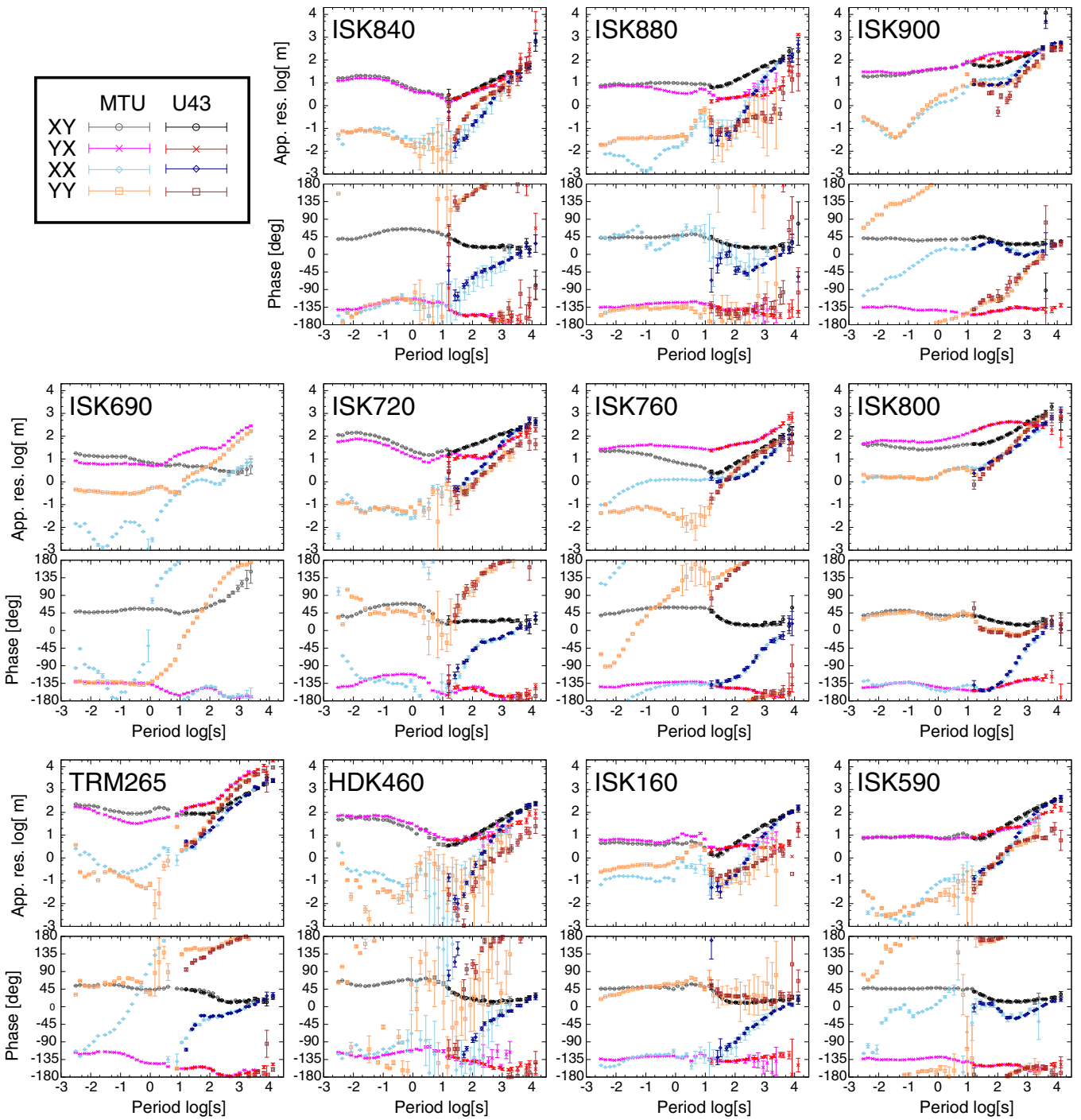

Figure 2. Sounding curves for the apparent resistivity and impedance phase at representative sites. (See Figure 1b for site locations.)

Figures 3−4 and 5−6 show maps of the apparent resistivity and impedance phase, respectively, at representative periods. The apparent resistivity of the off-diagonal components increases from 10 to 1000 Ωm with increasing period from 0.1 to 2000 s. The apparent resistivity is notably low at the center of the lowland and increases with increasing distance from the center. The impedance phase is larger than 45° in the central lowland and decreases on both sides. Additionally, the phase generally decreases for periods longer than 100 s. These features imply an overall resistivity structure in which a conductive layer that is thickest at the center of the lowland spans the surface and an underlying resistive basement exists beneath it.

Figure 7 shows the phase tensor ellipses for the responses and the real part of the induction vector (Parkinson convention). The phase tensor is defined as $\Phi = \mathbf{X}^{-1}\mathbf{Y}$, where **X** and **Y** are the real and imaginary parts of the MT impedance tensor, respectively [*Caldwell et al*., 2004]. The major and minor axes of the phase tensor ellipses represent Φ_{max} and Φ_{min}, respectively. The skew angle β, which represents the asymmetry of the phase tensor, has a large absolute value under a 3-D structure. The induction vector generally points toward a conductive structure, and its magnitude reflects the contrast of the resistivity.

The induction vector for periods shorter than 10 s has a small magnitude and a heterogeneous direction. In this period band, the phase tensor ellipse is an almost perfect circle, and its skew angle is nearly zero. These facts imply that the surface structure is nearly homogeneous. However, for periods longer than 10 s, large induction vectors point to the central lowland, and the phase tensors elongate in the NNW-SSE direction. This likely means that a conductive zone striking in the NNW-SSE direction spreads in the lowland. In the same band, the skew angle reaches ±20°, suggesting strong three-dimensionality. The induction vector points to the Pacific Ocean and the Sea of Japan for period bands of 10–1000 and >1000 s, respectively. *Yamaya et al*. [2009] demonstrated that the induction vector and phase tensor for periods longer than 10 s near the Shikotsu caldera region could be well explained by a regional 3-D structure causing current channeling, which consists of a thick conductive layer beneath the lowland and seawater distributed among the Pacific Ocean and Sea of Japan.

4. Three-Dimensional Modeling

4.1. Forward Modeling to Evaluate the Regional Pattern of the MT Responses

The measured phase tensor and induction vector imply a regional effect caused by the thick conductive sediments and seawater surrounding the study area. Prior to inversion modeling, in order to evaluate the regional effect on the MT response, 3-D forward models were studied while assuming a simple resistivity structure. The forward calculation part of WSINV3DMT [*Siripunvaraporn et al*., 2005; *Siripunvaraporn and Egbert*, 2009] estimated MT responses and magnetic transfer functions for 16 periods between 0.025 and 8197 s. The 3-D calculation region consisted of cuboid cells and had dimensions of 62, 62, and 38 cells in the *x* (north), *y* (east), and *z* directions (vertical), respectively. The minimum cuboid cell was designed to have a horizontal 2 km square base with a vertical thickness of 20 m. The entire model had dimensions of 684, 684, and 340 km in the *x*, *y*, and *z* directions, respectively.

First, a model assuming a land area (100 Ωm) and seawater was considered (Figure 8a). Because the calculated apparent resistivity and impedance phase showed a horizontally smooth change for all periods (supporting information Figure S1), the mesh design for the model was considered to be appropriate for expressing the bathymetry. The calculated phase tensor and induction vector are shown in Figure 8a. Although the induction vectors pointed to nearby coasts for periods of less than 363 s, they also pointed roughly westward for a period of 2000 s. This was caused by the deep bathymetry of the Sea of Japan, which rapidly deepens (>3000 m) in the western region about 200 km from the study area (Figure 1a). This induction vector tendency disagrees strongly with that produced via measured data. In addition, the ellipticity and azimuth of the phase tensor are also different. Thus, the regional pattern of the phase tensor and induction vector cannot be explained by the sea effect alone.

Next, we examined the model to demonstrate the observed induction vector for periods of 63.9–363 s, which implied a shallow conductor elongated in the NNW-SSE direction. The model included a conductive layer at depths between 0.05 and 3 km, as shown in Figure 8b. The calculated responses were similar to the observed responses for periods of 63.9 and 363 s, while the induction vector in the southern region of the study area did not point to the coast. However, the calculated responses for 2000 s made little sense.

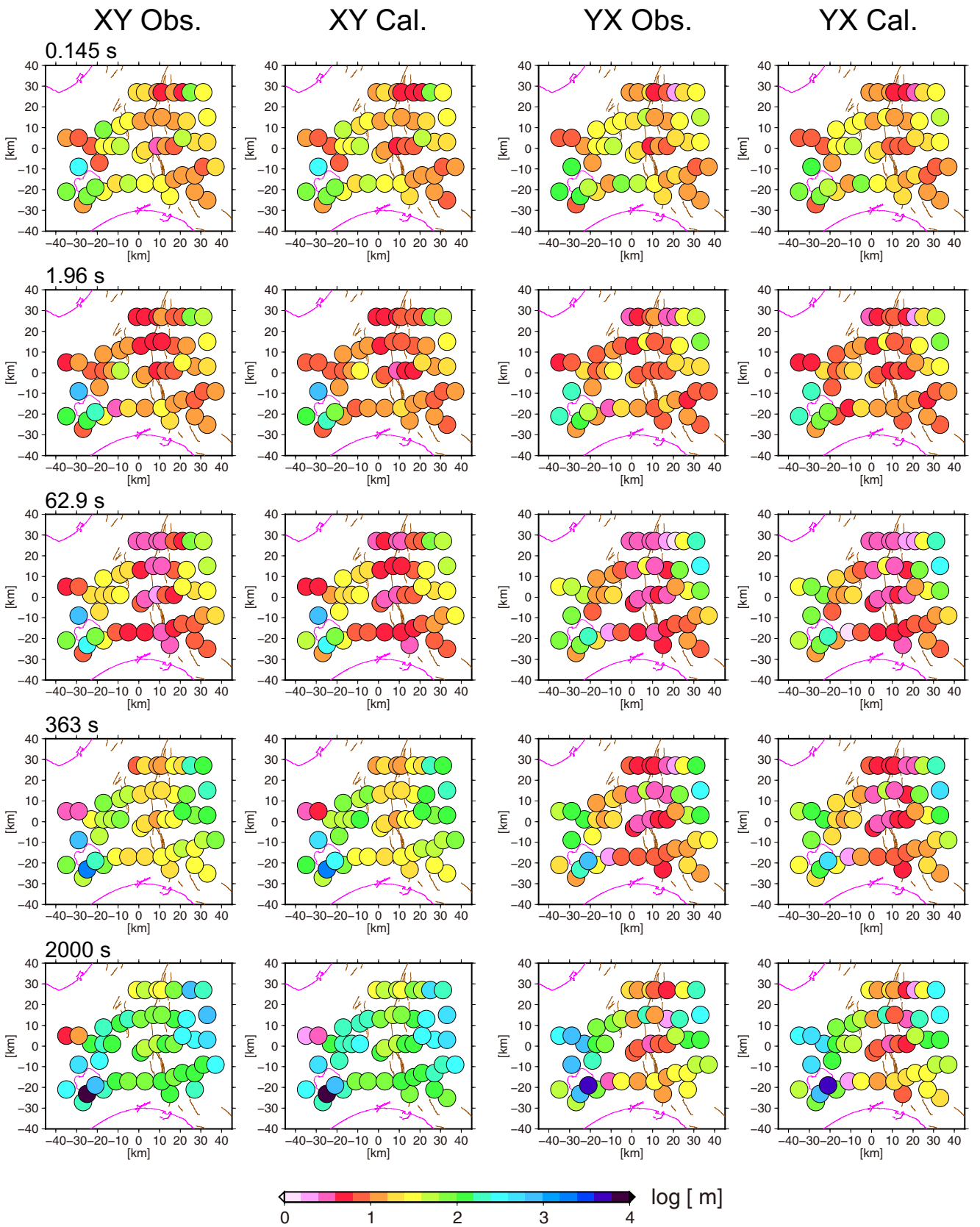

Figure 3. Apparent resistivity map of observed (Obs.) and calculated (Cal.) responses for representative periods. The off-diagonal components (Z_{XY} and Z_{YX}) of the impedance tensor are shown. Noisy observed data have been removed.

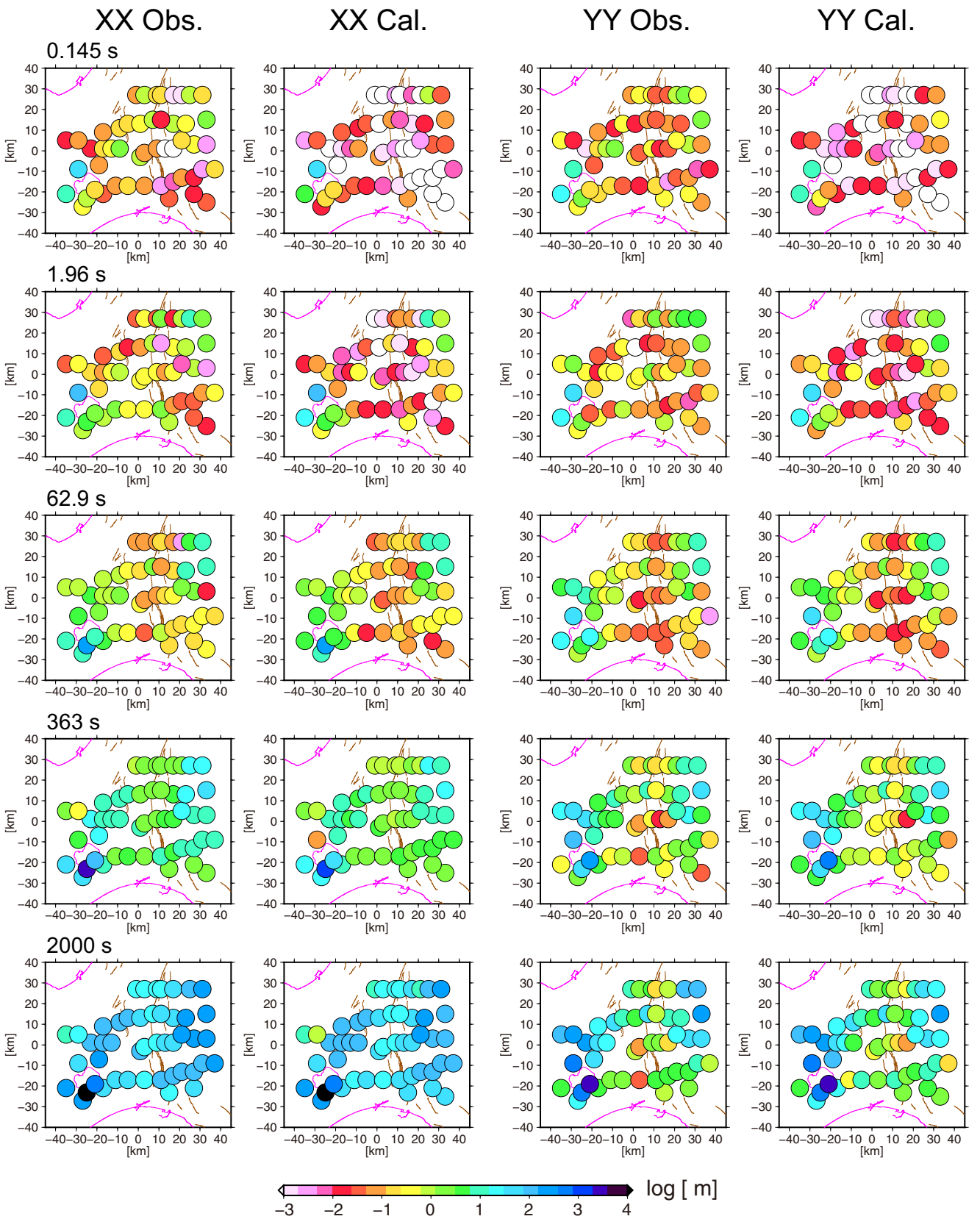

Figure 4. Apparent resistivity map of observed (Obs.) and calculated (Cal.) responses for representative periods. The diagonal components (Z_{XX} and Z_{YY}) of the impedance tensor are shown. Noisy observed data have been removed.

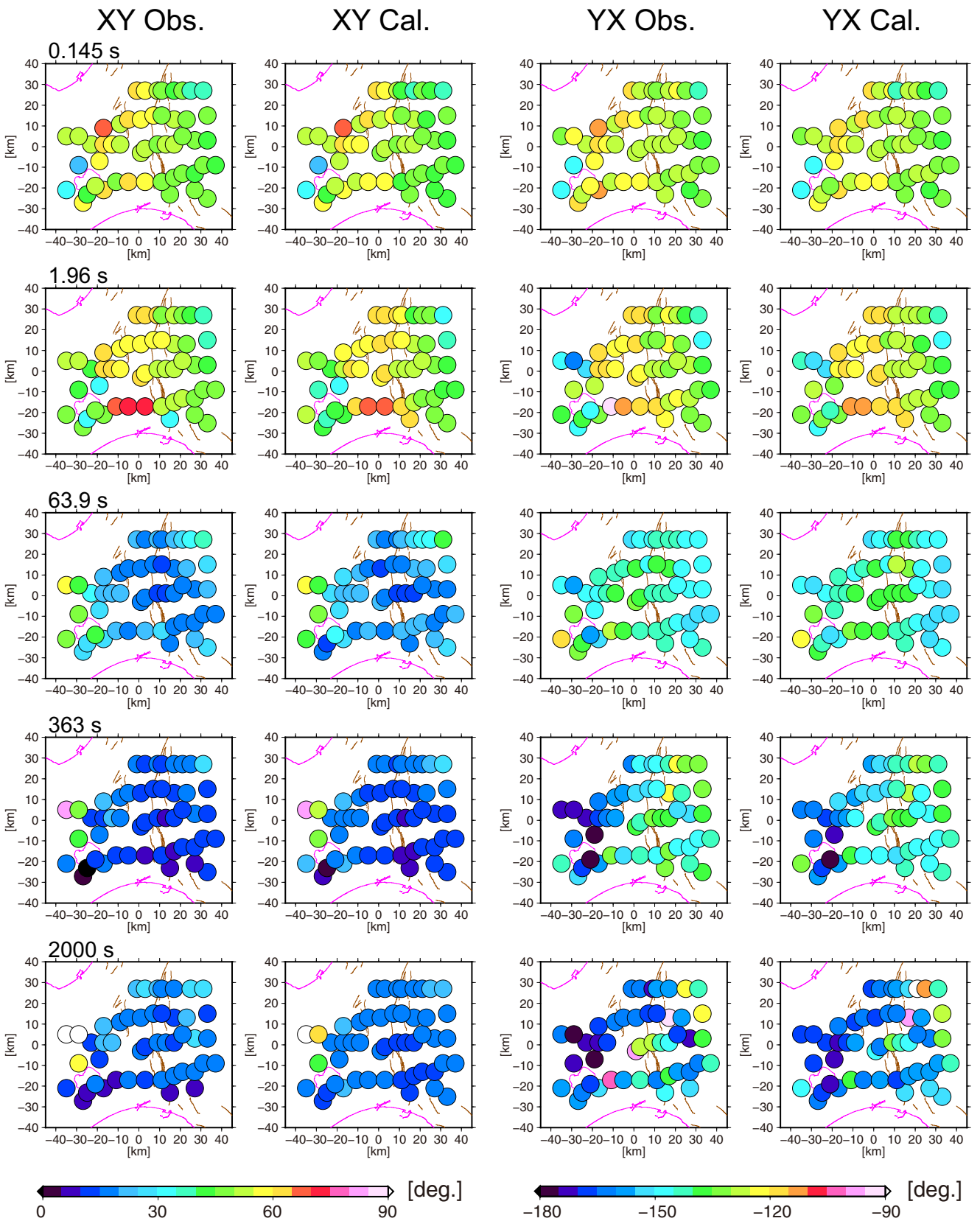

Figure 5. Impedance phase map of observed (Obs.) and calculated (Cal.) responses. The off-diagonal components (Z_{XY} and Z_{YX}) of the impedance tensor are shown. Noisy observed data have been removed.

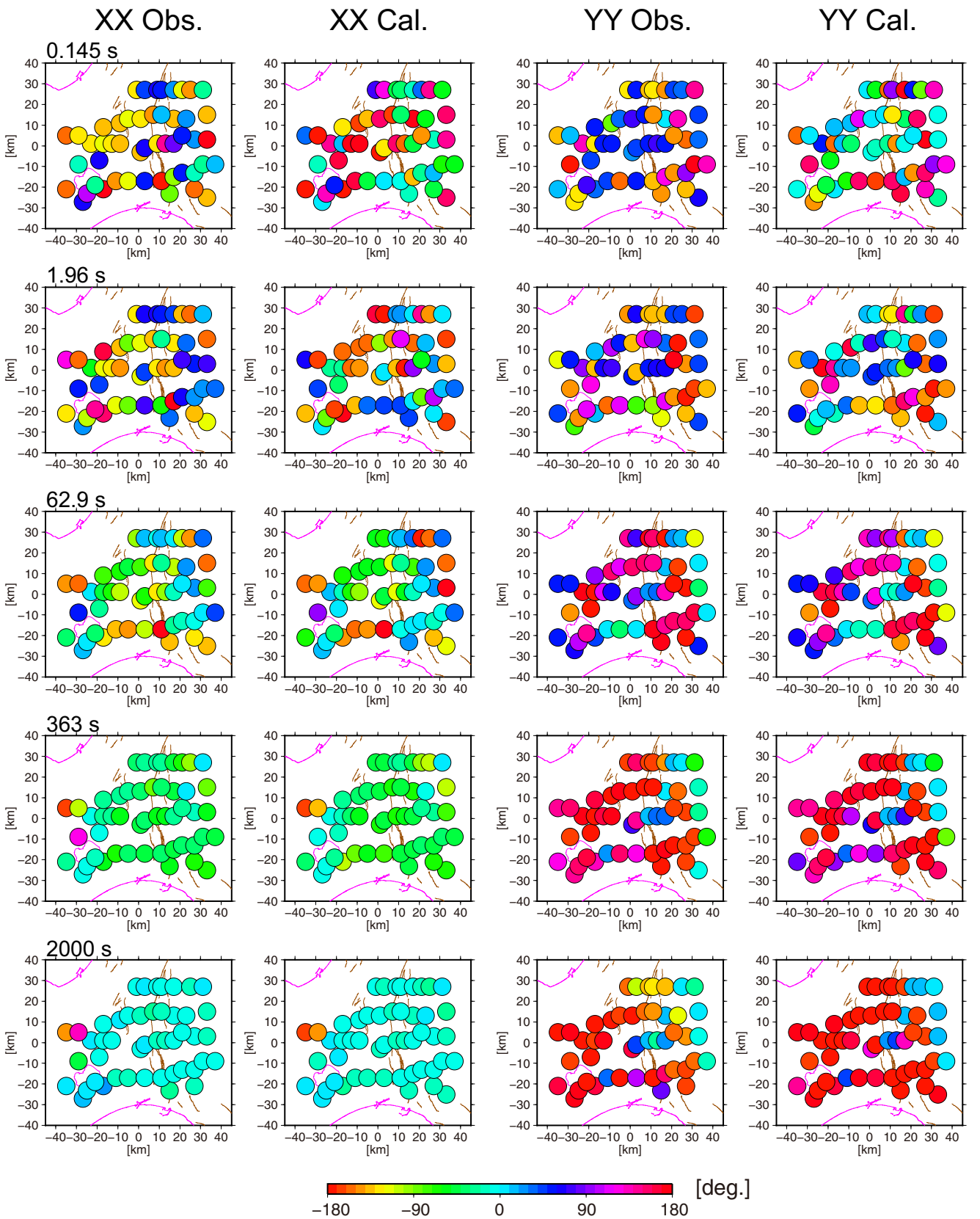

Figure 6. Impedance phase map of observed (Obs.) and calculated (Cal.) responses. The diagonal components (Z_{XX} and Z_{YY}) of the impedance tensor are shown. Noisy observed data have been removed.

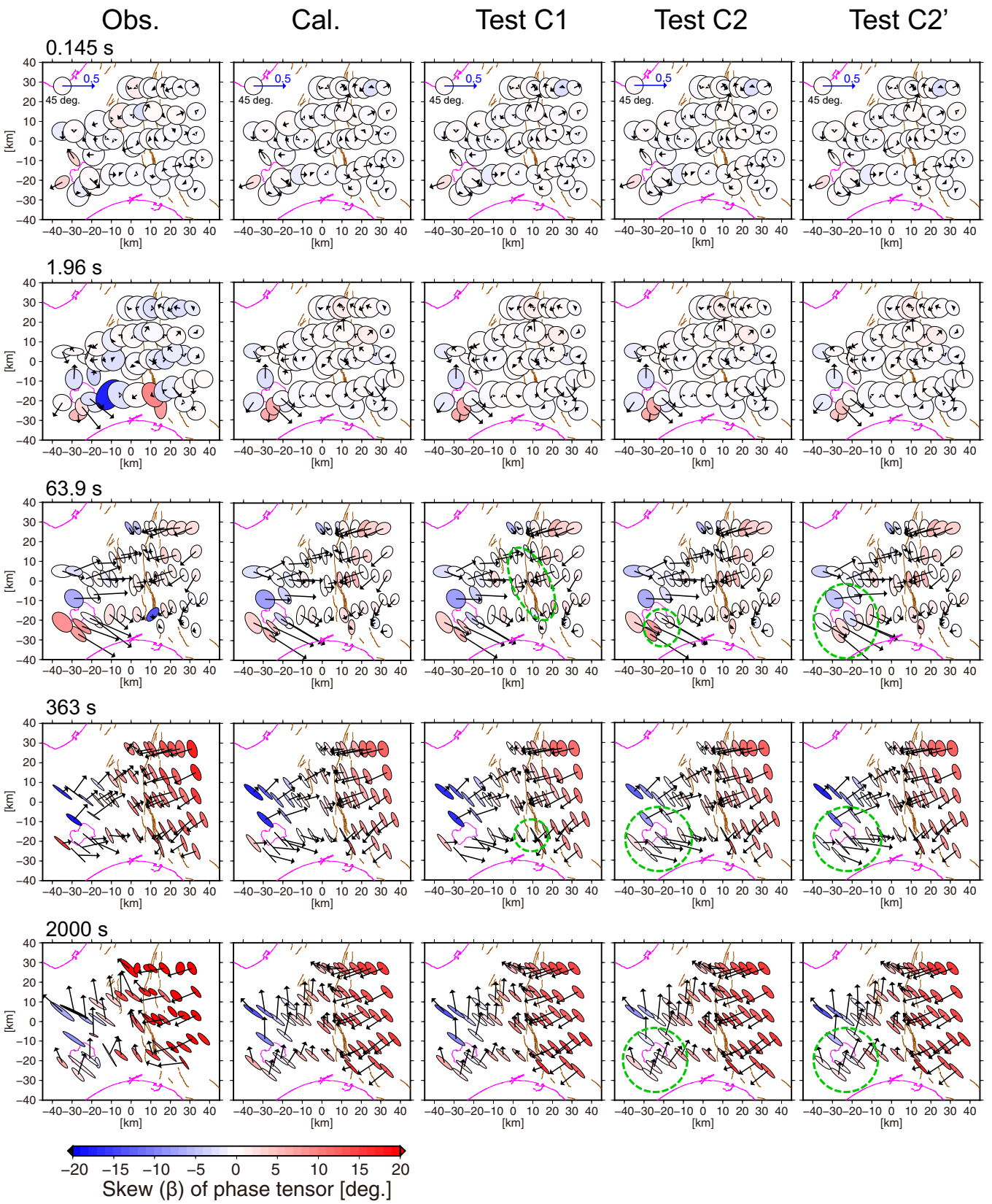

Figure 7. Induction vectors (Parkinson convention) and phase tensor ellipses for representative periods. The color of the ellipses indicates the skew angle β for the phase tensor. Obs. and Cal. indicate observed values and values calculated using the inverted model responses, respectively. Noisy observed data have been removed. Tests C1, C2, and C2′ show the calculated responses for a model with a conductor resistivity of 100 Ωm. The dashed green circle indicates the region in which a response change occurs.

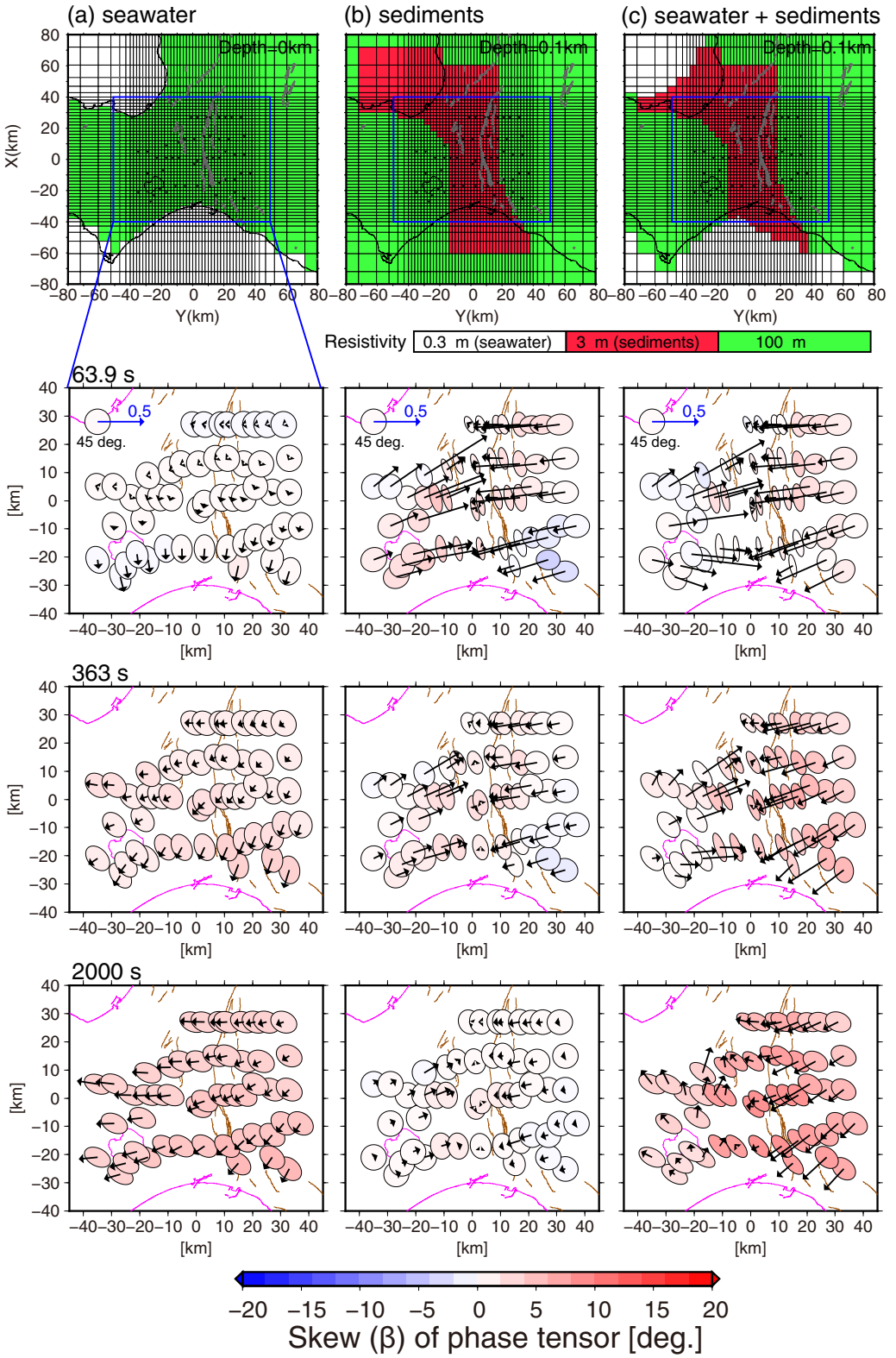

Figure 8. (top row) Plan views of resistivity model used in the forward calculations. (Other rows) calculated phase tensor ellipses and real induction vectors (Parkinson convection).

Finally, a model including both seawater and a conductive layer was examined (Figure 8c). The calculated phase tensor and induction vector well explained the measured data even though the skew (β) and magnitude of the induction vector were underestimated. These might depend on the detailed distribution of the conductor and resistivity contrasts among the conductive layer, seawater, and the other lands. Therefore, the measured regional pattern was probably caused by the combination of the two seas and the conductive channel connecting them. However, because it is difficult to consider such structure in two-dimensional (2-D) analysis, we decided that 3-D inversion is the most appropriate method for estimating the resistivity structure in the study area.

4.2. Inversion

The 3-D inversion analysis of the obtained MT data was conducted using the 3-D inversion program WSINV3DMT that was based on a data space Occam's inversion scheme [*Siripunvaraporn et al*., 2005; *Siripunvaraporn and Egbert*, 2009]. Data for 16 periods between 0.025 and 8197 s from the 50 wideband sites were selected; 20 of these sites also include longer-period data. The input data contained four components of the impedance and two components of the magnetic transfer function. Because each input value was a complex number, the input data contained a total of 12 components. The model settings were the same as those used in the forward modeling. The common initial and prior models, which define the resistivities of the land and seawater as 100 and 0.3 Ωm, respectively, were used (same as Figure 8a). The resistivity of the seawater was fixed during the inversion. The root-mean-square (RMS) residuals of the observed and calculated responses were 16.0 in the initial model, allowing a 5% error floor.

The inversion analysis was conducted in three stages. The first-stage inversion was performed with three smoothing parameters ($\tau = 2.5$, 5, and 10 with $\delta x = \delta y = \delta z = 0.1$) in the model covariance matrix [*Siripunvaraporn and Egbert*, 2000; *Siripunvaraporn et al*., 2005], to determine an appropriate smoothing parameter. The inversions with $\tau = 2.5$, 5, and 10 reduced the RMS residuals to 2.68 after six iterations, 2.66 after four iterations, and 2.90 after five iterations, respectively (supporting information Figure S2). Although the RMSs of the models with $\tau = 2.5$ and 5 were almost equivalent, we selected the smoother model with $\tau = 5.0$ as the first-stage model on the basis of Occam's inversion so that the smoothest model with plausible data misfit level was selected as the best model [*Constable et al*., 1987]. This first-stage resistivity model was used as the new initial and prior models for the second-stage inversion. The second-stage inversion reduced the RMS residual to 1.88 after five iterations. This procedure was repeated as the third stage, during which the RMS residual finally converged to 1.59 after four iterations. The calculated apparent resistivity and impedance phase from the third-stage model are shown in Figures 3−6, and 11. Additionally, the calculated induction vector and phase tensor are shown in Figure 7. The calculated data accurately describe all components of the observed data. Plan and section views of the resistivity model are shown in Figures 9 and 10, respectively.

The features of the resistivity model (Figures 9 and 10) are as follows. The conductive layer ($<$10 Ωm) extends from the surface to a depth of approximately 7 km. This layer is quite thin in the western region and thickens toward the eastern region. Below the conductive layer, the resistive layer (300 Ωm) continues to the bottom of the model. In the resistive layer, two remarkable conductors named C1 and C2 are present beneath the ITFZ and Shikotsu caldera, respectively (Figures 9 and 10).

4.3. Sensitivity Tests

Considering the locations of C1 and C2 beneath the active fault and volcano, respectively, these conductors may be important in the interpretation of the resistivity structure in this region. A simple sensitivity test was performed by forward modeling to examine these conductors. The resistivity of C1 was set to 100 Ωm, which is similar to the surrounding resistivity. Considering the model with this resistivity of C1, the MT responses were calculated, as shown in Figure 11a. This caused the RMS residual to increase to 1.65. The calculated apparent resistivity and phase in this test did not agree well with the observed and best fit curves. The disagreement was significant at station ISK160, while only small changes were found at the other stations. The calculated induction vector at the stations around C1 pointed in different directions from those for the observed and best fit data for periods longer than 100 s. Because a significant change was observed at station ISK160, we tested the first-stage inversion again with the measured data while excluding the ISK160 data. The resulting model showed a conductor at a position very near C1, although the estimated

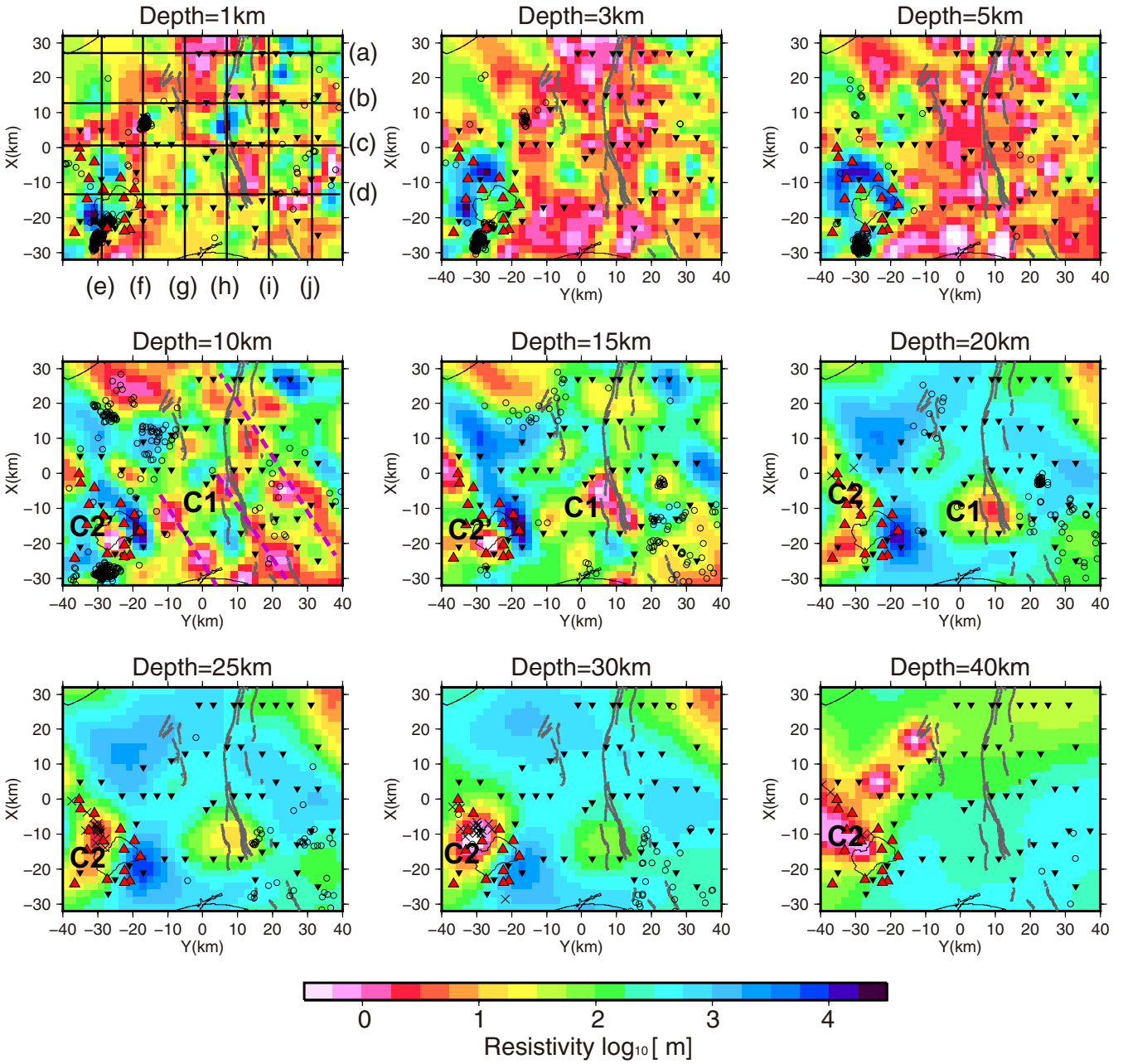

Figure 9. Plan views of 3-D resistivity model at various depths. Inverted triangles represent MT sites. Red triangles represent Quaternary volcanoes. Gray lines trace active faults. Purple dashed lines indicate conductive chains (see text). Open circles and crosses indicate hypocenters of ordinary earthquakes and DLFs, respectively, that occurred between 1997 and 2014, as determined by the JMA. Lines labeled as (a)–(j) correspond to the resistivity cross sections shown in Figure 10.

resistivity was somewhat higher than that for the final model (supporting information Figure S3). This implied that C1 could be supported by numerous measured data, and that the data for station ISK160 could effectively constrain C1.

The tests for the conductor beneath the Shikotsu caldera were divided by a depth 16 km to the deeper part (C2) and shallower part (C2′). Similar to C1, when the resistivity of C2 was set to 100 Ωm, the RMS residual increased to 1.70. The fit of the apparent resistivity and phase was also poor at several sites (Figure 11b). The phase tensor and induction vector did not explain the measured data for a period band above 100 s when compared with the inverted model (Figure 7). The test for C2′ showed the most significant change in the MT responses (Figure 11c), increasing the RMS residual to 2.10. The phase tensor and induction vector

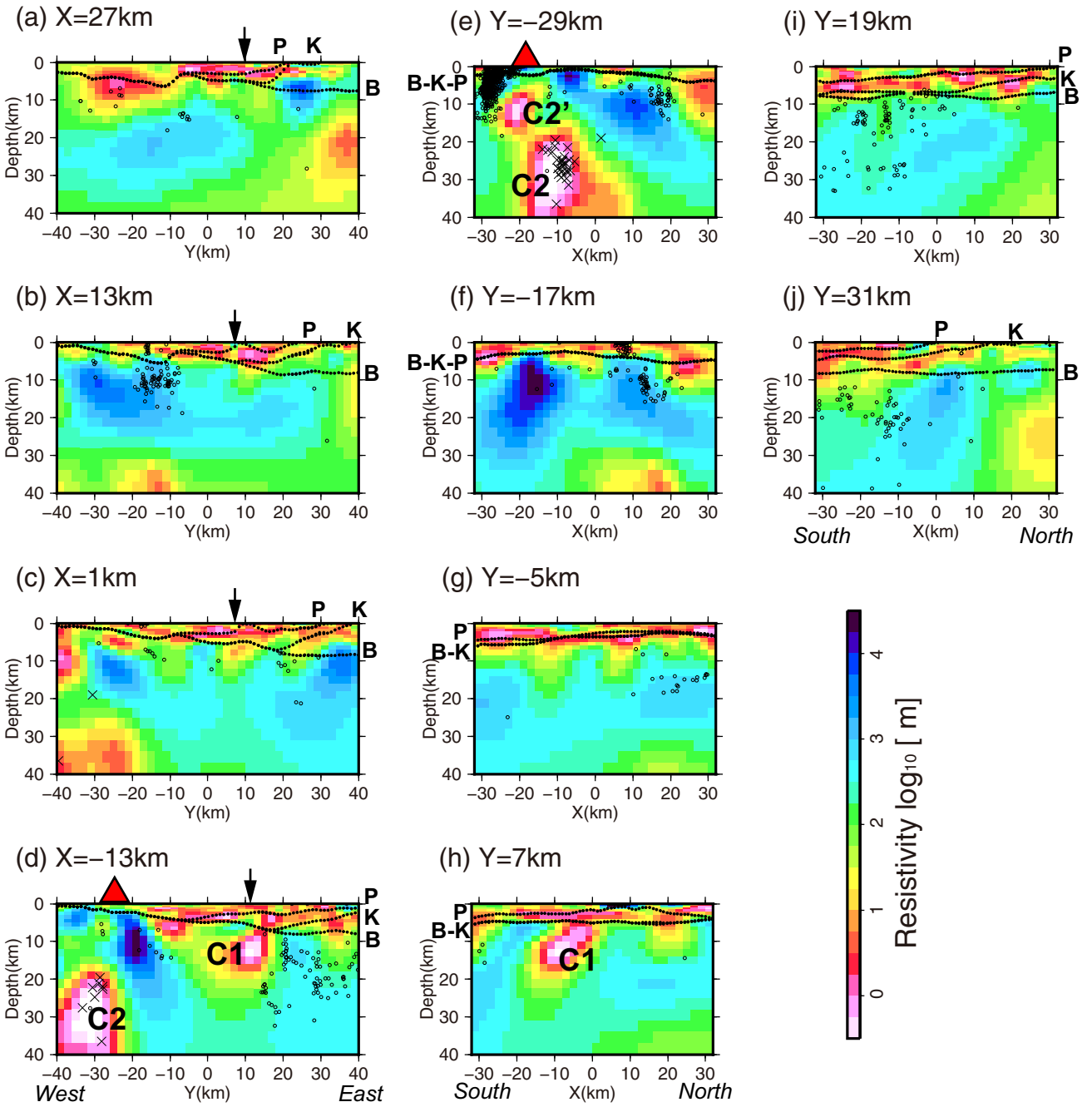

Figure 10. Cross sections of 3-D resistivity model. Sections labeled as (a)–(j) correspond to the lines shown in Figure 9. The red triangle indicates the location of the Shikotsu caldera. The downward-pointing arrows indicate the location of an active fault. Black dotted lines labeled as P, K, and B represent the top surfaces of the Paleogene, Upper Cretaceous, and Basement formations, respectively. Hypocenters are represented by the same symbols as in Figure 9.

became more inconsistent (Figure 7). Therefore, these conductors were necessary to explain the measured data, even though the changes were generally small in all the tests.

The conductors were also estimated at positions similar to C1, C2 and C2′, even in the first-stage inversion with different smoothing parameters (supporting information Figure S2), so it is unlikely that the conductors were artifacts caused by inappropriate smoothing. However, the volume and resistivity of the conductors seem to depend on the smoothing parameter τ. In addition, it is possible that the MT data has poor sensitivity for an extremely low resistivity at the center of the conductors because the response changes in the forward modeling tests were not particularly large. In order to constrain the reliable resistivity range for the

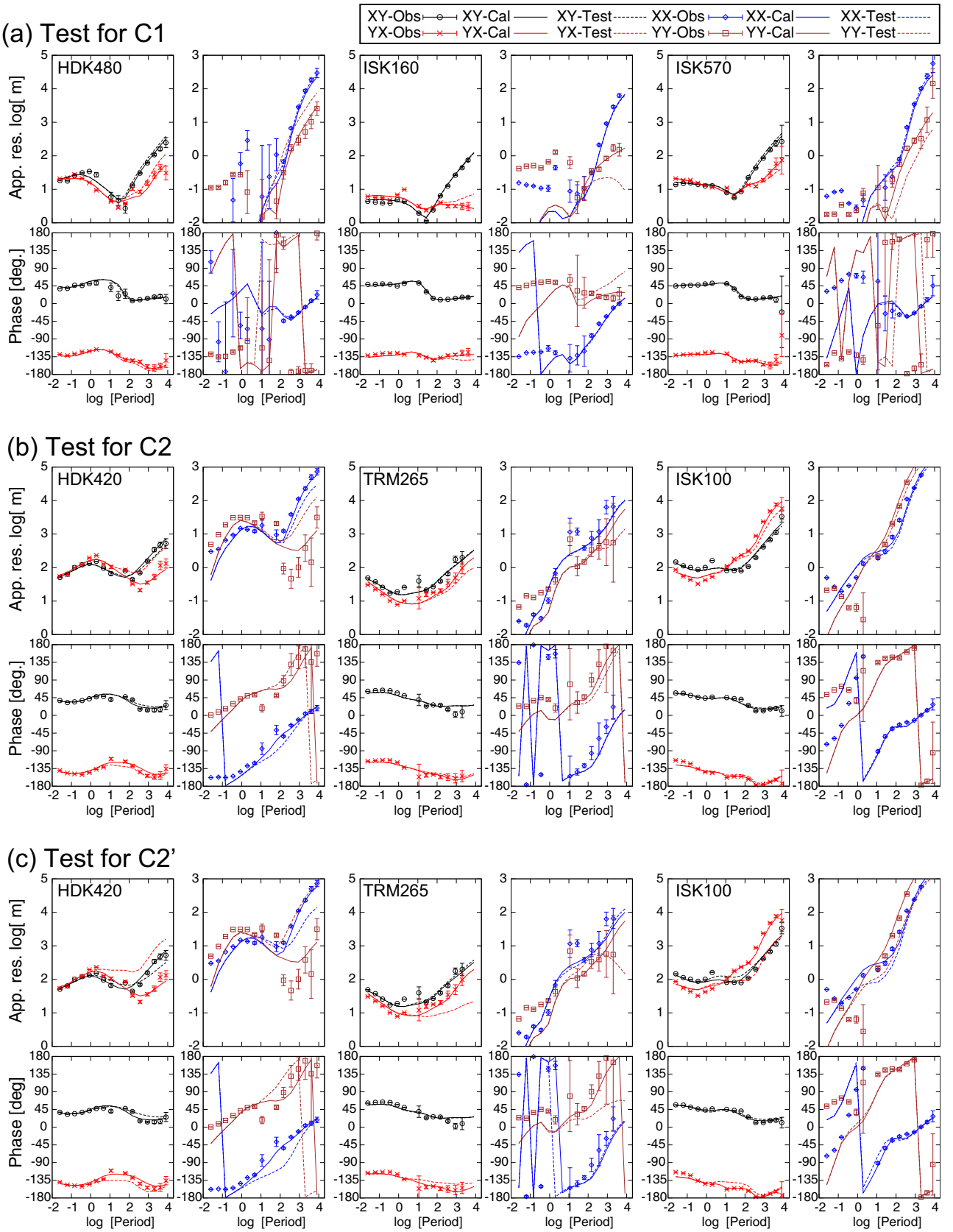

Figure 11. Sensitivity test results of apparent resistivity and impedance phase for (a) C1, (b) C2, and (c) C2′. Dots with error bars, solid lines, and dashed lines represent the observed (Obs), best fit (Cal), and test (Test) responses, respectively.

Table 1. RMS Residuals for the Sensitivity Test Models

Conductor	Inverted Model	1 Ωm	3 Ωm	10 Ωm	30 Ωm	100 Ωm	300 Ωm
C-1	1.591	1.592	1.597	1.612	*1.630*	*1.645*	*1.655*
C-2	1.591	1.591	1.593	1.602	*1.635*	*1.698*	*1.751*
C-2′	1.591	1.591	1.600	*1.648*	*1.790*	*2.059*	*2.362*

[a]Note: The values in the first row indicate filled resistivities in the tests. RMS residuals indicating significant differences compared with the inverted model are italicized. The significances are based on a *F* test with a 95% confidence level. All models have 9599 degrees of freedom.

conductors, additional sensitivity tests after *Ichihara et al.* [2014] were performed for C1, C2, and C2′. These tests consisted of forward calculations with conductor resistivity settings of 1, 3, 10, 30, 100, and 300 Ωm. Table 1 shows the RMS residuals for these tests. We evaluated the global model RMS residuals for each calculation with the aid of an *F* test. The variances of residuals (square of RMS) of the best fit and tested models were compared. The degree of freedom was equal to all the fitting parameters, defined by $E\times P\times S-1=12\times16\times50-1=9599$, where *E*, *P*, and *S* denoted the numbers of response component, period, and measurement station, respectively. A probability (α) with respect to an *F* distribution was obtained from a variance and degree of freedom. We, adopting a 95% confidence level, judged significance with $\alpha<0.025$. Thus, the RMS residual larger than 1.623 was determined to be significantly different from the best fit one.

Based on this *F* test, C1, C2, and C2′ with resistivities higher than 30, 30, and 10 Ωm, respectively, produced significantly worse RMS residuals compared with the best model. In this sense, even though the best fit resistivity was less than 1 Ωm, a more resistive C1, C2, or C2′ of up to 30, 30, or 10 Ωm is used to fit the data equally. Furthermore, we performed some constrained inversions by fixing the resistivities of C1, C2, and C2′ as 30, 30, and 10, respectively. The results showed lower resistivities than the fixed ones at the outer edge of the fixed areas, or anomalously low resistivities of less than 0.1 Ωm at the nonfixed conductor. Such strange structures were considered to be unrealistic. Additionally, although the whole RMS residuals were reduced to equivalent values with the best fit model, curve fittings became worse at specific stations. This constrained inversion trial also supported the conductive anomalies at C1, C2, and C2′. Therefore, we interpret the resistivity structure in the following discussion based on the condition that the resistivity for the conductors C1, C2, and, C2′ is lower than 30, 30, and, 10 Ωm, respectively.

5. Discussion

5.1. Overall Interpretations of Resistivity Structure

The conductive layer (<10 Ωm) lies at the surface (Figures 9 and 10). This layer is not found in the western region and is 5–7 and 10 km thick in the central and eastern regions of the lowland, respectively. Comparing the seismic velocity structure compiled from explorations and logged data [*Yoshida et al.*, 2007], the bottom of this conductive layer is consistent with the top of the Upper Cretaceous (Figure 10). Thus, this layer corresponds to sedimentary rocks younger than the Paleogene.

The resistive layer (>300 Ωm) is present under the conductive layer. The resistive layer suggests a brittle upper crust because the Conrad depth was estimated to be approximately 20 km [*Katsumata*, 2010] and seismicity is concentrated in this layer (Figure 10). This layer tends to deepen and thicken toward the southeast. This tendency corresponds to the seismic velocity structure, which indicates that the interpreted crust rapidly thickens toward the east [*Iwasaki et al.*, 2004]. Furthermore, the characteristics of the resistive layer are in accordance with seismic tomography results, thereby suggesting that the crust belonging to the northeastern Japan arc is pushed down at the western side of the Hidaka collision zone [*Kita et al.*, 2010].

5.2. Conductor Beneath the Ishikari-Teichi-Toen Fault Zone

The depth of conductor C1, which has a resistivity of less than 30 Ωm, is estimated to be 5–15 km beneath the ITFZ (Figures 9 and 10). Because C1 exists fully in the Cretaceous basement, it is not considered to be an extension of the surface conductive layer, but an independent structure. High-temperature rocks, the presence of aqueous fluids, and partial melts in rocks can cause low resistivity. However, because the resistivity of dry rocks is always above 10 Ωm even if the highest temperature of 1000°C is assumed [*Kariya and Shankland*, 1983], high-temperature rocks alone cannot explain the resistivity of C1. Furthermore, it is considered difficult for partial melts to exist in the upper-middle crust in a nonvolcanic region showing a low heat flow [*Tanaka*, 2004] and a large solidus depth [*Okubo*, 1998]. In addition, the *P* wave velocity estimated

by seismic tomography indicated the presence of a slow structure near C1 relative to that of the surroundings [*Ichiyanagi et al*., 2012]. Therefore, a realistic interpretation of C1 is the presence of aqueous fluids reducing the resistivity. An MT study in the backarc of the northeastern Japan found similar midcrustal conductors beneath the thrust zone, which were interpreted as fluids accommodated by the enhanced porosity due to local stress accumulation [*Ogawa et al*., 2001].

A plan view at a depth of 10 km (Figure 9) shows several conductive spots ($<$30 Ωm) aligned in the NNW-SSE direction, as indicated by dashed lines. *Kurita and Yokoi* [2000] suggested the presence of a pull-apart basin generated under the transpression field in the late Pliocene (Figure 1b). The parallel conductive chains may indicate a damaged zone of vestigial faults forming the outer edge of the pull-apart basin. Based on an application of a dislocation model, *Tamaki et al*. [2010] reported that the right-lateral faults with lengths exceeding 30 km explained the formation of the pull-apart basin. The positions of the assumed faults in their model correspond to those of the conductive chains. A possible interpretation of this correspondence is that the conductive spots represent trapped fluids in the high-porosity damaged zone where fault fractures develop at a high rate. C1 shows a particularly low resistivity and large volume in comparison with other spots. In addition, a horst structure that formed under the transpression field in the late Pliocene was also recognized near C1 [*Kurita and Yokoi*, 2000]. Therefore, C1 may correspond to a highly fractured zone filled by fluids. This implies that the damaged zone developed with a strong heterogeneity and that fluids in this zone may have caused the heterogeneous crustal strength in this region.

5.3. Conductor Beneath the Shikotsu Caldera

C2 and C2′, which have resistivities of less than 30 and 10 Ωm, respectively, extend downward from a depth of 5 km to over 40 km beneath the Shikotsu caldera. The Shikotsu caldera is a Quaternary volcano activated 40,000–50,000 years ago [*Yamagata*, 1994], and its postcaldera cones remain active. The conductive column from C2 to C2′ suggests a fluid path or reservoir, which can cause volcanic activity at the surface. Because C2 extends deeper than the Moho, which has a depth of approximately 30 km [*Katsumata*, 2010], the conductive column penetrates from the upper mantle to the crust.

In the northeastern Japan arc, the mantle wedge upwelling flow, which was caused by dehydration from the subducting Pacific Plate, rises up from the deep backarc to the Moho beneath the volcanic front, and then the melted and aqueous fluids constituting this flow accumulate there or intrude into the crust [*Hasegawa et al*., 2005]. The Li/Cl ratio of the deep ground water exceeds 0.001 in the Shikotsu region, suggesting that slab-derived or magmatic aqueous fluids upwell in this region [*Kazahaya et al*., 2015]. Furthermore, *Okubo* [1998] estimated that the solidus depth is less than 30 km in this region, suggesting that partial melting could occur in the lower crust. Therefore, C2 is interpreted as aqueous fluids and/or partial melts intruding from the upper mantle into the crust.

Deep low-frequency earthquakes (DLFs) occur mostly at the upper edge of C2 (Figures 9 and 10). A DLF occurring in a deep part of a volcanic region may be related to magma migration under ductile conditions [*Ukawa*, 2007]. Assuming that C2 indicates partial melting, the DLFs in this region may be accompanied by magma migration into the crust. Additionally, DLFs can be related to the migration of aqueous fluids dehydrated from melts [*Hasegawa et al*., 2005]. Saline water and silicate melt can have a resistivity of lower than 1 Ωm, depending on their salt concentration and temperature [*Nesbitt*, 1993; *Gaillard and Marziano*, 2005]. Considering the resistivity of bulk rock, a resistivity below 30 Ωm would be realistic for a region that includes aqueous fluids and partial melts. Although the resistivity alone cannot be used to determine which cause is more likely, the conductive column indicates magmatic fluids, and C2 and C2′ are interpreted as the upwelling path and reservoir of these fluids, respectively.

The plan view at a depth of 40 km (Figure 9) shows additional conductors in the northeastern region of C2. However, in this region, there are no DLFs, and the conductors do not extend upward. Thus, the conductors in this region might indicate the accumulation of magmatic fluids under the Moho without intrusion into the crust.

5.4. Possible Mechanism for Strain Concentration in the Ishikari Lowland

In inland earthquake zones, conductors suggesting the presence of fluids in the lower crust beneath the fault zone have been found in many MT studies [e.g., *Ogawa et al*., 2001; *Ogawa and Honkura*, 2004; *Tank et al*., 2005; *Uyeshima et al*., 2005; *Yoshimura et al*., 2008; *Wannamaker et al*., 2009; *Ichihara et al*., 2014]. These

results are in accordance with the model proposed by *Iio et al*. [2002, 2004], which indicates that a weak zone permitting plastic deformation in the lower crust causes a strain concentration in the upper crust above the deformation, resulting in the occurrence of an earthquake as a brittle fracture. However, because the conductors beneath the Ishikari Lowland, such as C1, and other conductive spots are located in the upper crust, the model by *Iio et al*. [2002, 2004] cannot be applied to the mechanisms for strain concentration and earthquake generation in the study area. Furthermore, although most studies have suggested that fluids in the lower crust are likely supplied by slab-derived fluids [e.g., *Wannamaker et al*., 2009; *Ichihara et al*., 2014], there is no fluid path from the deeper parts of the study area except in the volcanic region. *Kato et al*. [2006] studied the mechanism for the 2004 Mid-Niigata Prefecture earthquake (M_{JMA} 6.8) and suggested that ductile deformation in the upper crust due to thick soft sediments reaching a depth of 10 km was strongly related to the occurrence of this earthquake. Similarly, the sediments in the Ishikari Lowland are also very thick, reaching a depth of 10 km in the eastern region. Additionally, the conductive spots indicating aqueous fluids in the basement suggest the strongly heterogeneous distribution of the crustal strength. Therefore, it is possible that the heterogeneously distributed ductile zones in the upper crust cause the strain to concentrate in the lowland. The basement appears to have rapidly risen beneath the ITFZ. Such a heterogeneous boundary of the dynamic properties can cause a stress concentration that brings about the conditions necessary for an inland earthquake [*Ichihara et al*., 2008]. The episodic intrusion of fluids from a saturated zone, such as C1, to a relatively strong shallower part may trigger an earthquake within the ITFZ.

6. Conclusions

An MT survey was conducted based on an assumed 3-D resistivity structure in the Ishikari Lowland region, which is recognized as a strain concentration zone in Hokkaido, Japan. The surface conductive layer was attributed to thick sedimentary rocks younger than the Paleogene. The model indicated remarkable conductors beneath the ITFZ and the Shikotsu caldera, which were interpreted as fluid-rich zones. However, their origin and role in tectonic activity differed. The conductor beneath the ITFZ corresponds to aqueous fluids accumulating in the damaged zone related to the formation of pull-apart faults and horst. In contrast, the conductive column beneath the Shikotsu caldera corresponds to a path for magmatic fluids flowing from the upper mantle, which likely include partial melts.

The results of this study suggest that ductile deformations in the upper crust, rather than a weak zone in the lower crust, contributed to the strain concentration in this area. The soft thick sediments spanning the entire lowland region allow ductile deformation to occur. Furthermore, local fluid-rich zones located at a depth of 10–20 km result in a heterogeneous distribution of the crustal strength, which causes rapid changes in the basement depth. These thick sediments and the local presence of fluids in the basement both contribute to the strain concentration in the Ishikari Lowland.

Acknowledgments
We are grateful to Dr. H. Asanuma from the Fukushima Renewable Energy Research Institute of the National Institute of Advance Industrial Science and Technology (AIST) and Dr. S. Ito from the Research Institute of Geology and Geoinformation, AIST, for helpful discussions and suggestions. We are also grateful to two anonymous reviewers for their constructive comments, which helped us to improve the manuscript. Additionally, we would like to thank Mr. A. Suzuki, Mr. H. Yamashita, Dr. S.A.M. Abdallah, Mr. M. Oyama, Mr. T. Sasaki, and Dr. M. Matsumoto for their assistance in the field. We thank Dr. W. Siripunvaraporn for supplying his 3-D inversion code. The Kakioka Geomagnetic Observatory of the Japan Meteorological Agency (JMA) and the Geospatial Information Authority of Japan provided us with their continuous geomagnetic records from Kakioka and Esashi stations, respectively. This study was supported by the "Multidisciplinary Research Project for High Strain Rate Zones" of the Ministry of Education, Culture, Sports, Science and Technology (MEXT), Japan. The Ishikari-Yufutsu 3-D Model developed by the Active Fault Research Center, AIST, was used to create some figures. The "Active Fault Shape File" [*Nakata and Imaizumi*, 2002; product serial DAFM2775] was used to create some figures. The earthquake catalog used in this study was produced by the JMA in cooperation with MEXT. The catalog is based on seismic data provided by the National Research Institute for Earth Science and Disaster Prevention, JMA, Hokkaido University, Hirosaki University, Tohoku University, the University of Tokyo, Nagoya University, Kyoto University, Kochi University, Kyushu University, Kagoshima University, AIST, the Geographical Survey Institute, Tokyo Metropolis, Shizuoka Prefecture, Hot Springs Research Institute of Kanagawa Prefecture, Yokohama City, and the Japan Agency for Marine-Earth Science and Technology. Some figures were created using the Generic Mapping Tools [*Wessel and Smith*, 1998]. All the magnetotelluric data used in this paper are available; data can be requested by contacting YY (y.yamaya@aist.go.jp).

References

Caldwell, T., H. M. Bibby, and C. Brown (2004), The magnetotelluric phase tensor, *Geophys. J. Int.*, *158*, 457–469, doi:10.1111/j.1365-246X.2004.02281.x.

Chave, A. D., and D. J. Thomson (2004), Bounded influence estimation of magnetotelluric response functions, *Geophys. J. Int.*, *157*, 988–1006, doi:10.1111/j.1365-246X.2004.02203.x.

Constable, S. C., R. L. Parker, and C. G. Constable (1987), Occam's inversion: A practical algorithm for generating smooth models from EM sounding data, *Geophysics*, *52*, 289–300, doi:10.1190/1.1442303.

Earthquake Research Committee (2010), The long-term evaluation for the Ishikari-teichi-toen fault zone [in Japanese], Headquarters for Earthquake Res. Promotion, Tokyo. [Available at http://jishin.go.jp/main/chousa/katsudansou_pdf/06_ishikari-teichi.pdf.]

Gaillard, F., and G. I. Marziano (2005), Electrical conductivity of magma in the course of crystallization controlled by their residual liquid composition, *J. Geophys. Res.*, *110*, B06204, doi:10.1029/2004JB003282.

Gamble, T. D., W. M. Goubau, and J. Clarke (1979), Magnetotellurics with a remote magnetic reference, *Geophysics*, *44*, 53–68, doi:10.1190/1.1440923.

Geological Survey of Japan (2013), Quaternary Volcanoes of Japan database, Geol. Surv. Jpn., AIST, Tsukuba, Ibaraki. [Available at https://gbank.gsj.jp/volcano/index_e.htm.]

Hasegawa, A., J. Nakajima, N. Umino, and S. Miura (2005), Deep structure of the northeastern Japan arc and its implications for crustal deformation and shallow seismic activity, *Tectonophysics*, *403*, 59–75, doi:10.1016/j.tecto.2005.03.018.

Hasegawa, A., J. Nakajima, N. Uchida, T. Okada, D. Zhao, T. Matuzawa, and N. Umino (2009), Plate subduction and generation of earthquakes and magmas in Japan as inferred from seismic observations: An overview, *Gondowana Res.*, *16*, 370–400, doi:10.1016/j.gr.2009.03.007.

Hashimoto, M., and T. Tada (1988), Horizontal crustal movements in Hokkaido and its tectonic implications [in Japanese with English abstract], *J. Seismol. Soc. Jpn.*, *41*, 29–38.
Hirose, W., and M. Nakagawa (2000), Transition of Neogene arc volcanism in Central-Western Hokkaido, viewed from K-Ar ages, style of volcanic activity, and bulk rock chemistry [in Japanese with English abstract], *J. Geol. Soc. Jpn.*, *106*, 120–135, doi:10.5575/geosoc.106.120.
Ichihara, H., R. Honda, T. Mogi, H. Hase, H. Kamiyama, Y. Yamaya, and Y. Ogawa (2008), Resistivity structure around focal area of the 2004 southern Rumoi-Nanbu Earthquake (M6.1), *Earth Planets Space*, *60*, 883–888, doi:10.1186/BF03352841.
Ichihara, H., S. Sakanaka, M. Mishina, M. Uyeshima, T. Nishitani, Y. Ogawa, Y. Yamaya, T. Mogi, and K. Amita (2014), A 3-D electrical resistivity model beneath the focal zone of the 2008 Iwate-Miyagi Nairiku earthquake (M 7.2), *Earth Planets Space*, *66*, 50, doi:10.1186/1880-5981-66-50.
Ichiyanagi, M., et al. (2012), Seismic activity and crustal structure of Ishikari-Teichi-Toen active fault on the dense seismic observation [in Japanese], Programme and Abstracts P-121(155), the Seismological Society of Japan, Fall Meeting, Seismol. Soc. of Jpn, Tokyo.
Iio, Y., T. Sagiya, Y. Kobayashi, and I. Shiozaki (2002), Water-weakened lower crust and its role in the concentrated deformation in the Japanese Islands, *Earth Planet. Sci. Lett.*, *203*, 245–253, doi:10.1016/S0012-821X(02)00879-8.
Iio, Y., T. Sagiya, and Y. Kobayashi (2004), Origin of the concentrated deformation zone in the Japanese Islands and stress accumulation process of intraplate earthquakes, *Earth Planets Space*, *56*, 831–842, doi:10.1186/BF03353090.
Ishikawa, N., and M. Hashimoto (1999), Average horizontal crustal strain rates in Japan during interseismic period deduced from geodetic surveys (Part 2) [in Japanese with English abstract], *J. Seismol. Soc. Jpn.*, *52*, 299–315.
Ito, T. (2000), Crustal structure of the Hidaka collision zone and its foreland fold-and-thrust belt, Hokkaido, Japan [in Japanese with English abstract], *J. Jpn. Assoc. Pet. Technol.*, *65*, 103–109.
Iwasaki, T., K. Adachi, T. Moriya, H. Miyamachi, T. Matsushima, K. Miyashita, T. Takeda, T. Taira, T. Yamada, and K. Ohtake (2004), Upper and middle crustal deformation of an arc-arc collision across Hokkaido, Japan, inferred from seismic refraction/wide-angle reflection experiments, *Tectonophysics*, *388*, 59–73, doi:10.1016/j.tecto.2004.03.025.
Kariya, K. A., and T. J. Shankland (1983), Electrical conductivity of dry lower crustal rocks, *Geophysics*, *48*, 52–61, doi:10.1190/1.1441407.
Kato, A., S. Sakai, N. Hirata, E. Kurashimo, T. Iidaka, T. Iwasaki, and T. Kanazawa (2006), Imaging the seismic structure and stress field in the source region of the 2004 mid-Niigata prefecture earthquake: Structural zones of weakness and seismogenic stress concentration by ductile flow, *J. Geophys. Res.*, *111*, B08308, doi:10.1029/2005JB004016.
Katsumata, A. (2010), Depth of the Moho discontinuity beneath the Japanese islands estimated by travel time analysis, *J. Geophys. Res.*, *115*, B04303, doi:10.1029/2008JB005864.
Kazahaya, K., M. Takahashi, T. Kirita, K. Naito, and Y. Watanabe (2015), Spatial distribution of upwelling area of slab-derived aqueous fluids In Japan, *Geol. Surv. Jpn. Open File Rep.*, *616*, Geol. Surv. Jpn., AIST, Tsukuba, Ibaraki.
Kiminami, K., M. Komatsu, K. Niida, and N. Kito (1986), Tectonic divisions and stratigraphy of the Mesozoic rocks of Hokkaido, Japan [in Japanese with English abstract], *Monogr. Assoc. Geol. Collab. Jpn.*, *31*, 1–15.
Kimura, G. (1986), Oblique subduction and collision—Fore-arc tectonics of the Kuril arc, *Geology*, *14*(5), 404–407.
Kita, S., T. Okada, A. Hasegawa, J. Nakajima, and T. Matsuzawa (2010), Anomalous deepening of a seismic belt in the upper-plane of the double seismic zone in the Pacific slab beneath the Hokkaido corner: Possible evidence for thermal shielding caused by subducted forearc crust materials, *Earth Planet. Sci. Lett.*, *290*, 415–426, doi:10.1016/j.epsl.2009.12.038.
Kuniyasu, M., and Y. Yamada (2004), Structural styles of deep zones in southern central Hokkaido, northern Japan [in Japanese with English abstract], *J. Jpn. Assoc. Pet. Technol.*, *69*, 131–144.
Kurita, H., and S. Yokoi (2000), Cenozoic tectonic settings and a current exploration concept in southern central Hokkaido, northern Japan [in Japanese with English abstract], *J. Jpn. Assoc. Pet. Technol.*, *65*, 58–70.
Mogi and Hidaka 2000 MT Group (2002), Wideband MT survey in the Hidaka region [in Japanese], *Earth Mon. (Gekkan Chikyu)*, *24*, 485–487.
Nakata, T., and T. Imaizumi (2002), *Digital Active Fault Map of Japan*, Univ. of Tokyo Press, Tokyo.
Nesbitt, B. E. (1993), Electrical resistivities of crustal fluids, *J. Geophys. Res.*, *98*, 4301–4310, doi:10.1029/92JB02576.
Ogawa, Y., and Y. Honkura (2004), Mid-crustal electrical conductors and their correlations to seismicity and deformation at Itoigawa-Shizuoka Tectonic Line, Central Japan, *Earth Planets Space*, *56*, 1285–1291, doi:10.1186/BF03353352.
Ogawa, Y., et al. (2001), Magnetotelluric imaging of fluids in intraplate earthquake zones, NE Japan back arc, *Geophys. Res. Lett.*, *28*, 3741–3744, doi:10.1029/2001GL013269.
Okubo, Y. (1998), Analysis of thermal structure in the crust, in *Handbook of Geophysical Exploration (Methodology)* [in Japanese], edited by Soc. of Explor. Geophys. of Jpn., pp. 586–588, Soc. of Explor. Geophys. of Jpn., Tokyo.
Ohzono, M. (2013), Spatiotemporal strain distribution based on GPS network in Hokkaido induced by the 2011 off the Pacific coast of Tohoku Earthquake (Mw 9.0) [in Japanese with English abstract], *Geophys. Bull. Hokkaido Univ.*, *76*, 97–110, doi:10.14943/gbhu.76.97.
Sagiya, T., S. Miyazaki, and T. Tada (2000), Continuous GPS array and present-day crustal deformation of Japan, *Pure Appl. Geophys.*, *157*, 2303–2322, doi:10.1007/PL00022507.
Siripunvaraporn, W., and G. Egbert (2000), An efficient data-subspace inversion method for 2-D magnetotelluric data, *Geophysics*, *65*, 791–803, doi:10.1190/1.1444778.
Siripunvaraporn, W., and G. Egbert (2009), WSINV3DMT: Vertical magnetic field transfer function inversion and parallel implementation, *Phys. Earth Planet. Inter.*, *173*, 317–329, doi:10.1016/j.pepi.2009.01.013.
Siripunvaraporn, W., G. Egbert, Y. Lenbury, and M. Uyeshima (2005), Three-dimensional magnetotelluric inversion: Data-space method, *Phys. Earth Planet. Inter.*, *150*, 3–14, doi:10.1016/j.pepi.2004.08.023.
Tamaki, M., S. Kusumoto, and Y. Itoh (2010), Formation and deformation processes of late Paleogene sedimentary basins in southern central Hokkaido, Japan: Paleomagnetic and numerical modeling approach, *Island Arc*, *19*, 243–258, doi:10.1111/j.1440-1738.2009.00698.x.
Tanaka, A. (2004), Geothermal gradient and heat flow data in and around Japan (II): Crustal thermal structure and its relationship to seismogenic layer, *Earth Planets Space*, *56*, 1195–1199, doi:10.1186/BF03353340.
Tank, S. B., Y. Honkura, Y. Ogawa, M. Matsushima, N. Oshiman, M. K. Tuncer, C. Celik, E. Tolak, and A. M. Isikara (2005), Magnetotelluric imaging of the fault rupture area of the 1999 İzmit (Turkey) earthquake, *Phys. Earth Planet. Inter.*, *150*, 213–225, doi:10.1016/j.pepi.2004.08.033.
Ukawa, M. (2007), Low frequency earthquakes at Mount Fuji, in *Fuji Volcano* [in Japanese with English abstract], edited by S. Aramaki et al., pp. 161–172, Yamanashi Inst. of Environ. Sci., Fujiyoshida, Yamanashi.
Uyeshima, M., et al. (2005), Resistivity imaging across the source region of the 2004 Mid-Niigata Prefecture earthquake (M6.8), Central Japan, *Earth Planets Space*, *57*, 441–446, doi:10.1186/BF03351831.
Wannamaker, P. E., T. G. Caldwell, G. R. Jiracek, V. Maris, G. J. Hill, Y. Ogawa, H. M. Bibby, S. B. Bennie, and W. Heise (2009), The fluid and deformation regime of an advancing subduction system at Marlborough, New Zealand, *Nature*, *460*, 733–736, doi:10.1038/nature08204.

Wessel, P., and W. H. F. Smith (1998), New and improved version of Generic Mapping Tools released, *Eos Trans. AGU*, *79*, 579, doi:10.1029/98EO00426.

Yamagata, K. (1994), Tephrochronological study on the Shikotsu and Kuttara Volcanoes in Southwestern Hokkaido, Japan [in Japanese with English abstract], *J. Geogr.*, *103*, 268–285, doi;10.5026/jgeography.103.268.

Yamaya, Y., T. Mogi, and T. Hashimoto (2009), Effect of regional structure to MT response observed in Tarumai Volcano area, NE Japan, in *Proceedings of the 9th SEGJ International Symposium—Imaging and Interpretation, Sapporo, Japan* [CD-ROM], Soc. of Explor. Geophys. of Jpn., Tokyo.

Yoshida, K., M. Yoshimi, H. Suzuki, M. Morino, F. Takizawa, H. Sekiguchi, and H. Horikawa (2007), 3D velocity structure model of the Ishikari and Yufutsu sedimentary basins [in Japanese with English abstract], *Annu. Rep. Active Fault Paleoearthquake Res., Geol. Surv. Jpn., AIST*, *7*, 1–29.

Yoshimura, R., et al. (2008), Magnetotelluric observations around the focal region of the 2007 Noto Hanto Earthquake (Mj6.9), Central Japan, *Earth Planets Space*, *60*, 117–122, doi:10.1186/BF03352771.